Volume 13
Number 6
23 March 2026
Pages 2599–3130

Materials Horizons

rsc.li/materials-horizons

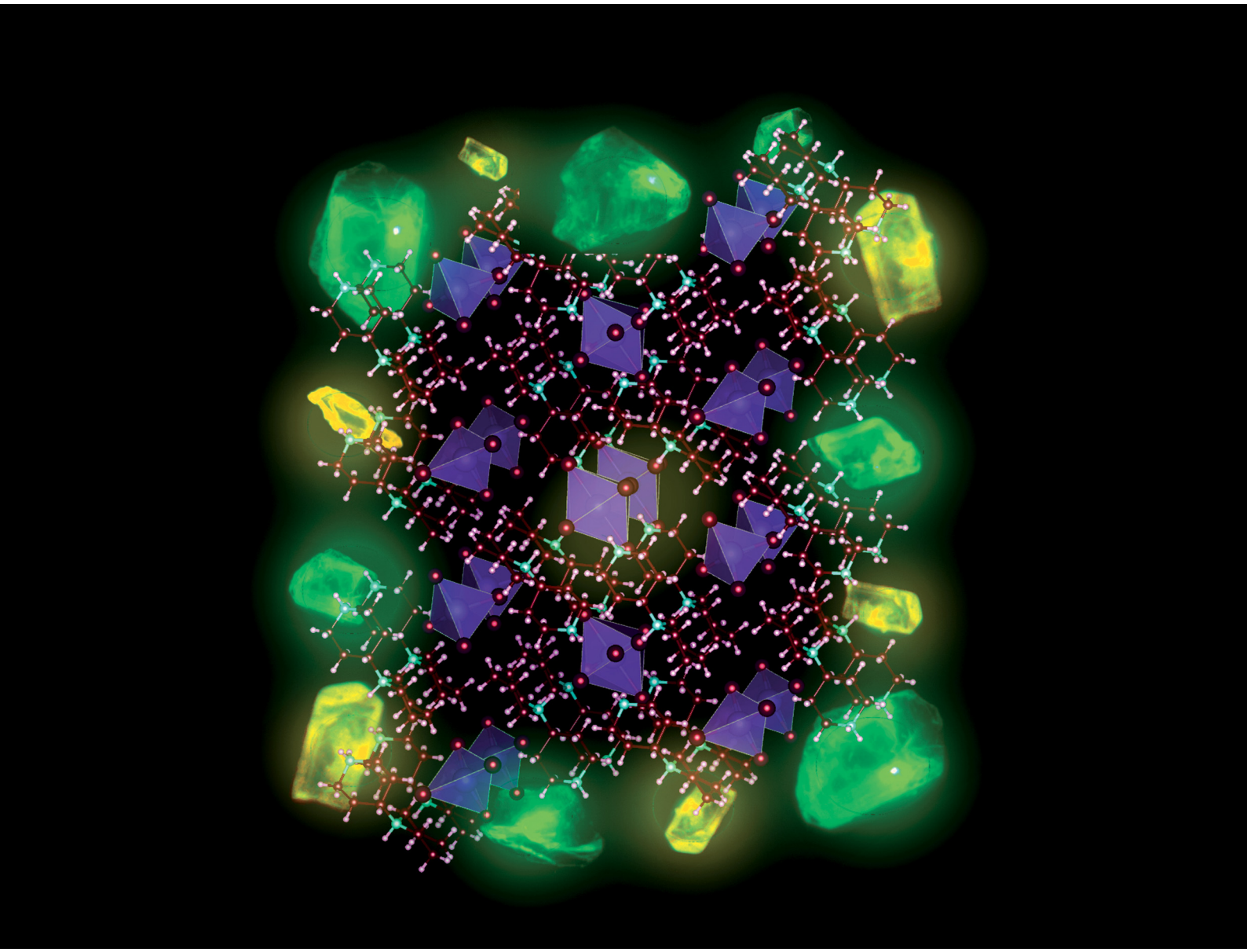

ISSN 2051-6347

ROYAL SOCIETY OF CHEMISTRY

COMMUNICATION

Vasudevanpillai Biju *et al.*

Isomeric organic–inorganic indium bromide single crystals with delayed and dual colour emission

Materials Horizons

ROYAL SOCIETY OF CHEMISTRY

COMMUNICATION

View Article Online
View Journal | View Issue

Cite this: *Mater. Horiz.*, 2026, 13, 2802

Received 5th December 2025,
Accepted 28th January 2026

DOI: 10.1039/d5mh02322j

rsc.li/materials-horizons

Isomeric organic–inorganic indium bromide single crystals with delayed and dual colour emission

Haichao Zhou,[a] Kiyonori Takahashi, †[ab] Takuya Okamoto, [ab] Jianguo Pan *[c] and Vasudevanpillai Biju *[ab]

Hybrid metal halides attract significant attention in materials science, chemistry, and photonics due to their attractive structural, electronic, and optical properties. However, zero-dimensional (0D) hybrid indium halides are still in their infancy. We report the first isomeric 0D indium halide single crystals showing green and delayed yellow emissions. Single-crystal X-ray structures reveal that these emissions originate from crystals with the molecular formula $(C_{10}H_{22}N_2)_4In_4Br_{20}$, consisting of organic ligands, $InBr_6$ octahedra, and $InBr_4$ tetrahedra. While both crystals carry eight corner-sharing and two face-sharing $InBr_6$ octahedra, the four face-sharing $InBr_4$ tetrahedra in the green-emitting isomer and two inner $InBr_4$ tetrahedra in the yellow-emitting isomer mark the crystal isomerism, leading to distinct optical properties. The green-emitting crystals exhibit short excitonic lifetimes, whereas the radiative recombination in the yellow-emitting crystals is delayed by several hundred nanoseconds and redshifted, indicating a self-trapped exciton behaviour with a large Huang–Rhys factor and high activation energy. The structural and optical properties of the isomeric single crystals offer insights into the importance of developing 0D metal halides with multi-colour and delayed emission for sensors, LEDs, and displays.

New concepts

We are working to develop metal halide single crystals with multicolor emission for optoelectronic applications. Using controlled crystal growth rates, we accidentally observed isomeric crystals emitting distinct green and yellow photoluminescence. These crystals are highly stable over a wide temperature range. During our photoluminescence microscopic and spectroscopic studies, we found that the emission colour is associated with distinct excited state lifetimes, with the yellow-emitting crystal showing delayed emission. Using temperature-controlled experiments from −193 to 30 °C, we could demonstrate the role of the self-trapped exciton and the activation energy associated with the yellow emission. These observations and results suggest opportunities to develop isomeric hybrid halide crystals in different dimensions into colourful, delayed-emission materials for optical sensors, luminescent displays, and brilliant LEDs.

Metal halides and halide perovskites transform semiconductor technology by emerging as key materials[1–5] for solar cells,[6–9] lasers,[10–12] LEDs,[13,14] and photodetectors.[15–17] Their exceptional properties, including low cost and straightforward fabrication methods, high optical absorption coefficients, tuneable direct band gaps, long charge-carrier diffusion lengths, low exciton binding energies, and high photoluminescence (PL) quantum yields (QYs), make them highly attractive for use in optical and photovoltaic devices. Single-crystal and polycrystal halide perovskite solar cells have achieved record-breaking efficiency gains, surpassing traditional silicon photovoltaics.[8] Also, tuning their bandgap through halide composition enables the fabrication of tandem and multi-junction solar cells for optimized energy harvesting.[9] Despite their extraordinary properties, poor stability and lead toxicity underscore the importance of developing stable and lead-free alternatives.[18–32]

Hybrid halides of tin,[18–20] antimony,[21,22] bismuth,[23,24] germanium,[25,26] copper,[27,28] and indium[29–32] receive considerable attention as lead-free alternatives; physicochemical stabilization and bandgap optimization remain open challenges. Several groups synthesized and investigated 0D hybrid metal halides to address these challenges. Among these, organic–inorganic copper and indium halides show promising advances.[27–32] Indium halides, such as caesium indium bromide ($CsInBr_x$), exhibit excellent optical properties, such as high oscillator strength, tuneable PL, and brilliant electroluminescence (EL),[33] and demonstrate outstanding stability.[34,35] Also, their fast, sensitive photo-response makes them ideal for high-performance X-ray detectors.[36] Importantly, indium makes these hybrid halides attractive for environmentally friendly and sustainable technologies. Therefore, there has been considerable interest in developing hybrid indium halides with tuneable optical and electronic properties through

[a] *Graduate School of Environmental Science, Hokkaido University, Kita 10, Nishi 5, Sapporo, Hokkaido 060-0810, Japan. E-mail: biju@es.hokudai.ac.jp*
[b] *Research Institute for Electronic Science, Kita 20, Nishi 10, Sapporo, Hokkaido 001-0020, Japan*
[c] *School of Materials Science and Chemical Engineering, Ningbo University, No. 818 Fenghua Road, Zhenhai, Ningbo, Zhejiang, China. E-mail: panjianguo@nbu.edu.cn*
† Current address: Department of Chemistry, Faculty of Advanced Science and Technology, Kumamoto University, Chuo-ku, Kumamoto 860-8555, Japan.

doping,[37–39] modifying organic ligands,[40–43] substituting halogens,[44–47] and inducing chirality.[48,49] Yet, the structure–property relationships of such crystals remain poorly understood.

We developed two 0D isomeric indium bromide single crystals with the formula $(C_{10}H_{22}N_2)_4In_4Br_{20}$, demonstrating distinct green and delayed yellow emissions. Although a crystal with the same precursors was reported by Yuan and coworkers,[41] which demonstrated brilliant yellow-orange emission, green-emitting crystals and the structural isomerism remained unknown. Also, the yellow-orange-emitting crystal showed a different molecular formula $[(C_{10}H_{22}N_2)_2In_2Br_{10}]$. However, the structural formula $[(C_{10}H_{22}N_2)_4In_4Br_{20}]$, determined from single-crystal X-ray diffraction (SCXRD) and elemental analysis, and the emission characteristics, determined from temperature-controlled steady-state and time-resolved PL measurements, of the isomeric crystals in the current work differ from those reported in ref. 41, which is attributed to differences in the synthesis conditions. Nevertheless, the empirical formula of the reported crystal matches those of the green- and yellow-emitting isomers. Structurally, these isomers feature four organic ligands, ten $InBr_6$ octahedra, and two inlaid or four face-shared $InBr_4$ tetrahedra per unit cell. Hereinafter, sharing means sharing of In atoms among unit cells. While both isomers contain eight corner-shared and two face-shared octahedra in their unit cells, the four face-shared $InBr_4$ tetrahedra in the green-emitting isomer and two unshared $InBr_4$ tetrahedra in the yellow-emitting isomer demonstrate crystal isomerism in indium halides. Interestingly, the green-emitting isomer exhibits a short PL lifetime (4.5 ns), whereas the yellow-emitting isomer shows a significantly delayed (>450 ns), redshifted, and enhanced PL.

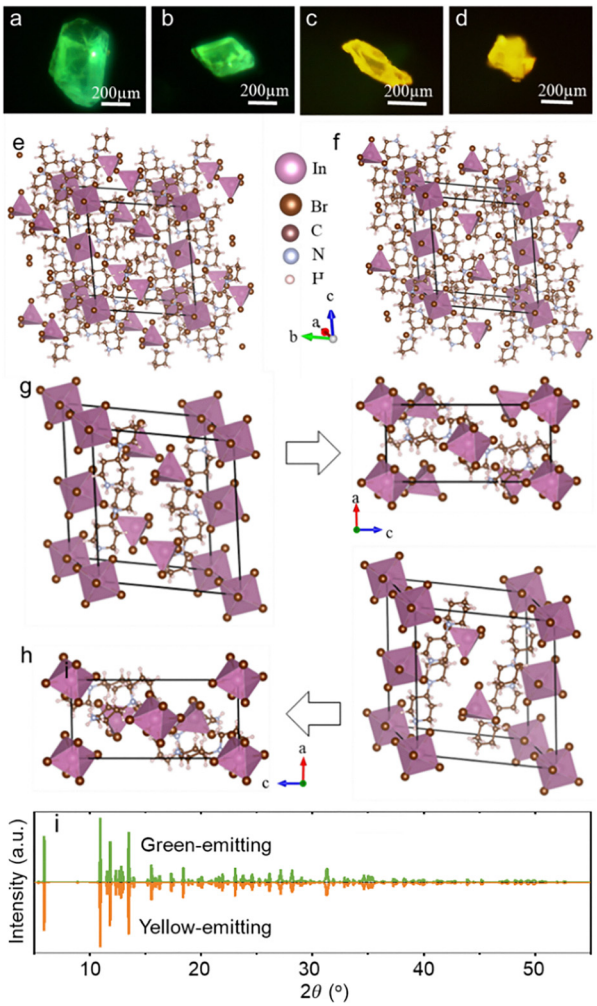

Fig. 1 SCXRD data of isomeric crystals. (a)–(d) PL images of $(C_{10}H_{22}N_2)_4In_4Br_{20}$ single crystals; SCXRD structures of (e) and (g) green- and (f) and (h) yellow-emitting isomers (the structural difference is shown in Fig. S1b and c (SI); and (i) PXRD patterns of the green- and yellow-emitting isomers.

Results and discussion

Preparation and characterization of crystals

We synthesized the isomeric crystals by controlling crystal nucleation and growth through cooling of a precursor solution containing 4-piperidinopiperidine ($C_{10}H_{20}N_2$, 97%), indium bromide ($InBr_3$, 99%), and aqueous hydrobromic acid (HBr, 47%). The precursor solution was prepared following a procedure reported in the literature[41] by dissolving 1.2 mmol of $C_{10}H_{20}N_2$ (201.9 mg) and 1.2 mmol of $InBr_3$ (425.4 mg) in 7.8 mL of aqueous (aq.) HBr solution at 25 °C, followed by heating to 120 °C with vigorous stirring. After 3 h, the temperature was decreased at 15 °C h^{-1} to 25 °C, predominantly providing large (50–200 μm) green-emitting crystals. Conversely, small-sized (10–50 μm) yellow-emitting crystals were formed in an identical precursor solution cooled at 10 °C h^{-1} from 120 to 25 °C. Nevertheless, a small fraction (<15%) of yellow-emitting crystals was present in the fast-cooled (15 °C h^{-1}) solution, and a small fraction (<20%) of green-emitting crystals was present in the slow-cooled (10 °C h^{-1}) precursor solutions. We attribute the crystal structure isomerism and differences in optical properties to differences in crystal growth rates at different cooling rates.

Photographs of the green- and yellow-emitting isomeric crystals are shown in Fig. 1a–d. We examined the crystal structures by single-crystal X-ray diffraction (SCXRD) and analysed them using VESTA software. The SCXRD structures of the isomeric crystals are shown in Fig. 1e–h, and the corresponding SCXRD patterns and the crystallographic parameters are shown in Fig. 1i, Table 1, and Table S1 (SI). The SCXRD patterns of the isomers are similar. We used a green-emitting isomer to extract the simulated XRD pattern from its SCXRD data and compared it with the experimental powder XRD pattern (PXRD), as shown in Fig. S1a (SI). Furthermore, we determined the elemental composition of the crystals from energy-dispersive X-ray spectroscopy (EDX) in conjunction with scanning electron microscopy (SEM). As shown in Fig. S2 (SI), the EDX spectrum of the green-emitting isomer demonstrated the indium to bromide ratio to be 1 : 5, which matches the stoichiometry (1 : 5) of the yellow-emitting crystal, indicating potential bromide vacancies in the green-emitting isomer. Additionally, we examined the thermal stability and organic ligand ratio in the isomeric crystals using differential thermal analysis (DTA). As shown in Fig. S3 (SI), both crystals demonstrated 20.5% weight

Table 1 Structural parameters of green- and yellow-emitting isomeric crystals

Parameters	Green-emitting crystal	Yellow-emitting crystal
Temperature (K)	298	298
Formula weight	1369.33	1369.33
Space group	$P\bar{1}$	$P\bar{1}$
Z	2	2
Crystal system	Triclinic	Triclinic
Unit cell dimensions	a = 7.726 Å, α = 75.916°, b = 15.542 Å, β = 89.357°, c = 16.970 Å, γ = 83.276°	a = 7.722 Å, α = 75.900°, b = 15.548 Å, β = 89.379°, c = 16.971 Å, γ = 83.338°
Volume (A^3)	1962.59	1962.42
Density (g cm^{-3})	2.3172	2.3174

loss in the 250–350 °C range, consistent with the formula derived from the SCXRD data.

Surprisingly, the isomers showed the same molecular (unit-cell) formula $[C_{10}H_{22}N_2)_4In_4Br_{20}]$ but different crystal structures (Fig. 1e and f). We arrived at this formula based on eight corner-shared $InBr_6$ octahedra and two face-shared $InBr_6$ octahedra, contributing two indium and twelve bromine atoms to the unit cells of both isomers (Fig. 1g and h). Also, the unit cells of the green-emitting isomer carry four face-shared $InBr_4$ tetrahedra (Fig. 1g). In contrast, the yellow-emitting isomer has two inlaid (unshared) $InBr_4$ tetrahedra (Fig. 1h). The four face-shared or two inlaid $InBr_4$ tetrahedra contribute two indium and eight bromine atoms to the unit cells of both isomers. The above $InBr_6$ octahedra, shared or unshared $InBr_4$ tetrahedra, and four unshared organic ligands provide the formula $(C_{10}H_{22}N_2)_4In_4Br_{20}$ for the isomeric crystals, demonstrating crystal-structure isomerism. Except for the difference in shared or unshared $InBr_4$ tetrahedra, the lattice parameters are comparable for the two types of crystals.

Optical properties

The different crystal structures contribute to different optical properties of the isomers, which were verified using PL images, absorption, PL, and excitation (PLE) spectra, and PL decays under different experimental and environmental conditions. The distinct green and yellow luminescence images of the crystals (Fig. 1a–d) were obtained under 405 nm laser (27.5 mW cm^{-2}) excitation using an inverted optical microscope. Fig. S4 (SI) displays the optical absorption spectra of the green- and yellow-emitting isomers, which show a distinct absorption cutoff near 300 nm. We calculated the optical band gaps of the green- and yellow-emitting isomers to be 3.54 eV and 3.68 eV, respectively, using Tauc plots (inset of Fig. S4, SI), which are comparable to that of the reported yellow-orange-emitting crystal (3.74 eV).[41] Normalized PL spectra of the isomeric crystals are shown in Fig. 2a, and the PLE spectra are shown in Fig. S5 (SI). The yellow-emitting isomer exhibited higher PL intensity than the green-emitting ones, irrespective of the crystal size or shape. Also, the green-emitting isomer showed a broad PL spectrum with an emission maximum at 530 nm and a full-width at half-maximum (FWHM) of 165 nm, whereas the yellow-emitting isomer showed an emission maximum at 590 nm and a FWHM of 150 nm. The redshifted

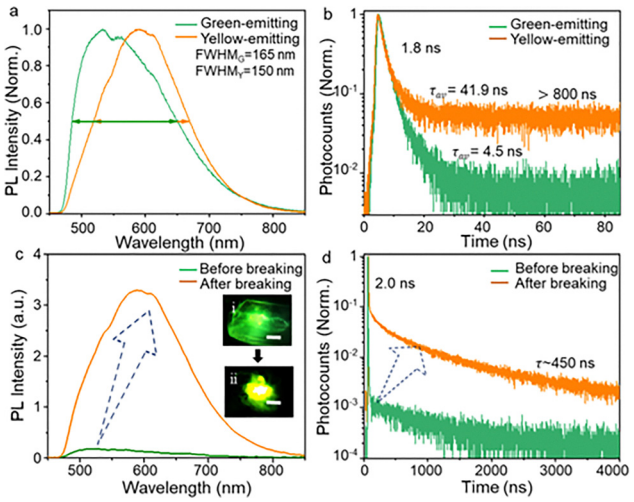

Fig. 2 Intrinsic and induced delayed dual emission. (a) PL spectra and (b) PL decay profiles of green and yellow emitting isomers. (c) PL spectra and (d) PL decay profiles of green-emitting isomer before and after cracking and photoirradiation (405 nm, 27.5 mW cm^{-2}).

emission of the yellow-emitting isomer suggests radiative recombination in the shallow band-edge or surface states.

To verify the relationships of the crystal structure to the surface-related emission from the yellow-emitting isomer and bromide vacancies in the green-emitting isomer, we estimated the PLQY and PL lifetimes of the crystals. The absolute PLQY for the green-emitting isomer was estimated to be 1.4%. The corresponding PLQY is 28% for the cracked, yellow-emitting, and photo-irradiated crystals. The low PLQYs support the hypothesis of a larger number of bromide vacancies in the green-emitting isomer than the yellow-emitting one. Furthermore, we recorded the PL decays of the isomers using a picosecond time-correlated single-photon counting (psTCSPC) microspectroscopic system equipped with a 405 nm ps laser (70 ps, 500 kHz) to understand the origins of the green and yellow emissions and relaxation kinetics of photoexcited states. Fig. 2b shows the PL decays of the isomeric crystals, which were fitted using the third exponential equation. Both isomers showed a fast relaxation component, with the decay constants in the 1.51×10^8–4.98×10^8 s^{-1} range for the green-emitting crystals and 1.83×10^8–5.52×10^8 s^{-1} for the yellow-emitting crystals. Interestingly, the yellow-emitting isomer exhibited an amplified and delayed decay component (1.25×10^6–2.18×10^6 s^{-1}), which is negligibly small for the green-emitting isomer. Based on the structural difference between the crystals, we attribute the delayed component to surface-related radiative recombination. The green-emitting isomer, with its four face-shared $InBr_4$ tetrahedra, shares more bromine atoms with neighbouring unit cells than the yellow-emitting one. Therefore, the green-emitting isomer can contain more surface bromine vacancies than the other, increasing the nonradiative recombination rate and rendering a short PL lifetime (τ_{av} = 4.5 ns), which is 41.9 ns for the yellow-emitting isomer.

While the green and yellow emissions are the intrinsic properties of the isomeric crystals, we observed a drastic

spectral shift (from green to yellow), a significant increase in PL intensity, and a long PL lifetime (Table S2, SI) when a green-emitting crystal was cracked and photoactivated. Conversely, such changes were not observed for the yellow-emitting isomer (Table S3, SI). To understand the origins of PL colour and lifetime changes, we examined PL spectra and decays of green-emitting crystals during cracking, with or without photoactivation. Here, a crystal sandwiched between two glass slides was cracked, and its PL properties were examined in real time. As soon as it was cracked and observed using a microscope and under a 405 nm laser (27.5 mW cm^{-2}), the emission colour changed from green to intense yellow (inset of Fig. 2c). The corresponding PL spectra are shown in Fig. 2c, showing a redshift in the spectral maximum from 532 to 592 nm.

To understand the effect of excitation power on the spectral red-shift, we recorded excitation power-dependent PL spectra of the green- and yellow-emitting isomers in the 5–55 mW cm^{-2} excitation range. PL spectral maxima are shown in Fig. S6a (SI). As the excitation power increased, the PL intensity of both crystals increased, with the yellow-emitting crystal exhibiting a more pronounced effect. The corresponding CIE (Commission Internationale de l'Eclairage) chromaticity coordinates are shown in Fig. S6b (SI), reflecting the excitation-induced PL evolution. The underlying mechanism responsible for the spectral shift is discussed below. Importantly, a long-lived (>450 ns) decay component became apparent after cracking and photoirradiation (Fig. 2d). The PL spectral redshift and long decay component indicate emission from low-lying states, suggesting that photoactivated surface-related states play a role in the intense yellow emission.

The PL spectra and decay constants for both isomers, as well as the high-intensity delayed emission from the yellow isomer, suggest that the band gaps and different radiative recombination rates are inherent to the crystal structures. We calculated the ratio (k_{rY}/k_{rG}) of the radiative recombination rates for the isomers as follows:[50] $\phi_G = \frac{k_{rG}}{k_{rG}+k_{nrG}}$ and $\phi_Y = \frac{k_{rY}}{k_{rY}+k_{nrY}}$. Also, $\tau_G = \frac{1}{k_{rG}+k_{nrG}}$ and $\tau_Y = \frac{1}{k_{rY}+k_{nrY}}$. Therefore, $\frac{\phi_Y}{\phi_G} = \frac{k_{rY}\times\tau_Y}{k_{rG}\times\tau_G}$, where ϕ_G, k_{rG}, k_{nrG}, and τ_G are the PLQY, the radiative rate, the nonradiative rate, and the average PL lifetime of the green-emitting isomers and ϕ_Y, k_{rY}, k_{nrY}, and τ_Y are the corresponding properties of the yellow-emitting isomer. From the PL lifetime values and PLQYs, we estimated the k_{rG} and k_{nrG} values to be 3.1 × 10^6 s^{-1} and 2.2 × 10^8 s^{-1}, respectively. The corresponding rate constants for the yellow-emitting isomer are estimated to be 6.7 × 10^6 s^{-1} (k_{rY}) and 1.7 × 10^7 s^{-1} (k_{nrY}). These rates support the enhanced and redshifted PL (Fig. 2c) from the photo-irradiated green-emitting isomer.

To further understand the origin of the emission dynamics in Fig. 2c and d, we examined the role of Br vacancies in the PL properties of pristine green-emitting and cracked crystals by soaking the crystals in a saturated NaBr solution. We observed a decrease in PL intensity (Fig. 3a) when a pristine isomer was immersed in the NaBr solution and examined under a low laser fluence (<10 mW cm^{-2}). Similarly, when we applied the NaBr solution to the cracked crystals, the PL intensity gradually decreased and blue-shifted (Fig. 3b, λ_{max} = 594 nm), suggesting that bromide vacancy filling suppresses exciton trapping to the yellow-emitting state. Relaxation processes in pristine and NaBr-treated crystals are summarized in Fig. 3c and d. The low PLQY and blue-shifted emission for the pristine crystal suggest a higher rate of nonradiative recombination (k_{nrG}) than k_{t1}. The intense and red-shifted emission from the cracked crystals suggests that the higher trapping rate, k_{t2}, than k_{nrG} and k_{rG} promotes the population of the yellow-emitting state. Also, the high-intensity yellow emission suggests $k_{nrD} < k_{t2} > k_{t1}$. Overall, the breaking-induced reconstruction of the energy-level structure suppresses the competitive nonradiative pathways (k_{nrG}) while promoting energy transfer, significantly red-shifting and enhancing the PL. Nevertheless, we considered and ruled out the photothermal effect on the green-to-yellow PL transition at different temperatures (Fig. S7, SI).

Furthermore, we examined the electronic structures of the crystals using first-principles DFT calculations. Fig. S8 (SI) shows band structures and density of states (DoS), revealing 2.71 and 2.73 eV band gaps for the green- and yellow-emitting isomers, respectively. Conversely, the DFT data do not correlate the PL properties with the electronic structures. Therefore, we assume that defect-assisted trapping–de-trapping and small lattice distortions play a significant role in the optical properties of the isomers.

Photoinduced and thermal PL dynamics

We investigated photoinduced and temperature-induced changes in the PL spectra and lifetimes of the green- and yellow-emitting isomers. For both, the PL intensity increased

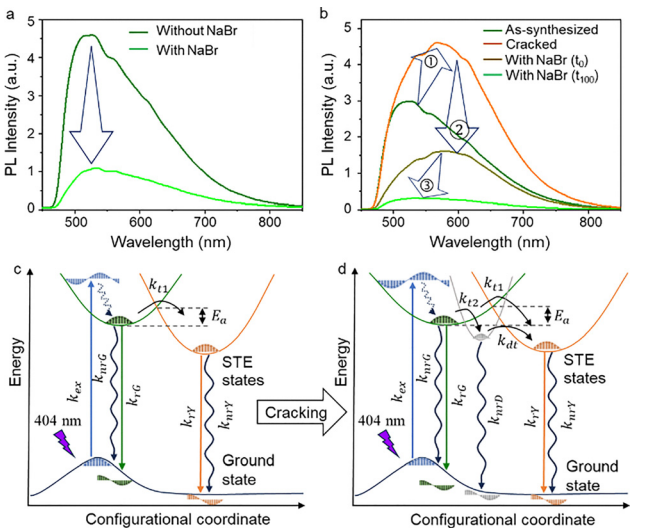

Fig. 3 Halide vacancy filling. PL spectra of as-synthesized green-emitting crystals (a) before and after NaBr treatment and (b) before and after NaBr treatment after cracking and photoactivation. The PL images in the upper and lower panels correspond to the spectra in 'a' and 'b'. (c) A scheme of the carrier/exciton recombination process in the green-emitting crystals (c) before and (d) after cracking.

with decreasing temperature from 80 to 300 K (Fig. S9, SI). Compared to the yellow-emitting isomer, the green-emitting isomer showed a pronounced blueshift in its PL spectrum (Fig. S9a and b SI). While the temperature-controlled PL spectra were measured by exciting the sample at 375 nm, the spectral features were independent of the excitation wavelength, as shown in Fig. S9c and d (SI). Although the exciton energy decreases by cooling or increases by heating due to low- or high-energy phonons, thermal relaxation to the lowest phonon state (band-edge) determines the PL spectral maxima. Furthermore, we compared the temperature-dependent FWHM (Fig. 4a and b) of the PL bands and estimated the Huang–Rhys factor (S), an indicator of electron–phonon interaction strength and self-trapped exciton (STE) formation, to assess the relationship between exciton–phonon coupling and PL properties of the isomeric crystals. Phonon-assisted STE formation can be evaluated using the following equation:[51,52]

$$\mathrm{FWHM} = 2.36\sqrt{S}\hbar\omega_{\mathrm{phonon}}\sqrt{\coth\frac{\hbar\omega_{\mathrm{phonon}}}{2k_{\mathrm{B}}T}}$$

where S is the Huang–Rhys factor, k_{B} is the Boltzmann constant, $\hbar$ is the Dirac constant, and ω_{phonon} is the phonon frequency. The S factor is 77.7 for the green-emitting isomer, which is 18.4 for the yellow isomer (Fig. 4a and b). These S values are significantly greater than those of standard crystals such as BA_6InCl_9 (S = 4.9)[34,35] and 3R-$ZnInS_4$ (S = 15),[53] indicating efficient phonon-assisted relaxation, which, for the green-emitting isomer, substantially helps overcome the energy barrier (E_{a}) between the green- and the yellow-emitting states, providing an appreciable PL spectral redshift and a longer PL lifetime.

To further understand exciton–phonon coupling, we analysed temperature-dependent broadening of the PL linewidth $\Gamma(T)$ using the established electron–phonon coupling model:

$$\mathrm{FWHM} = \Gamma(T) = \Gamma_0 + \Gamma_{\mathrm{ac}} + \Gamma_{\mathrm{LO}},$$

$$\Gamma(T) = \Gamma_0 + \gamma_{\mathrm{ac}}T + \gamma_{\mathrm{LO}} \times \frac{1}{e^{\frac{\hbar\omega}{k_{\mathrm{B}}T}}-1},$$

where Γ_0, Γ_{ac}, and Γ_{LO} are the inhomogeneous linewidths due to structural disorder, acoustic phonons, and longitudinal optical phonons. Also, γ_{ac} and γ_{LO} are the acoustic- and the optical-phonon coupling coefficients, and $\hbar\omega$ is the average optical phonon energy. Here, we fixed $\hbar\omega$ as a constant during the calculation of the S values (Fig. 4a and b). As shown in Fig. 4c and d, the green-emitting isomer exhibited a significantly greater γ_{LO} value than the yellow-emitting isomer, indicating much stronger exciton–optical phonon coupling, while γ_{ac} values are comparable. These results suggest that optical phonons broaden the PL spectrum of the green-emitting crystal and play a critical role in its exciton relaxation dynamics, whereas the yellow-emitting isomer is characterized by relatively weak electron–phonon coupling, where bromide vacancy-assisted trapping and further de-trapping into the yellow-emitting state govern the PL colour.

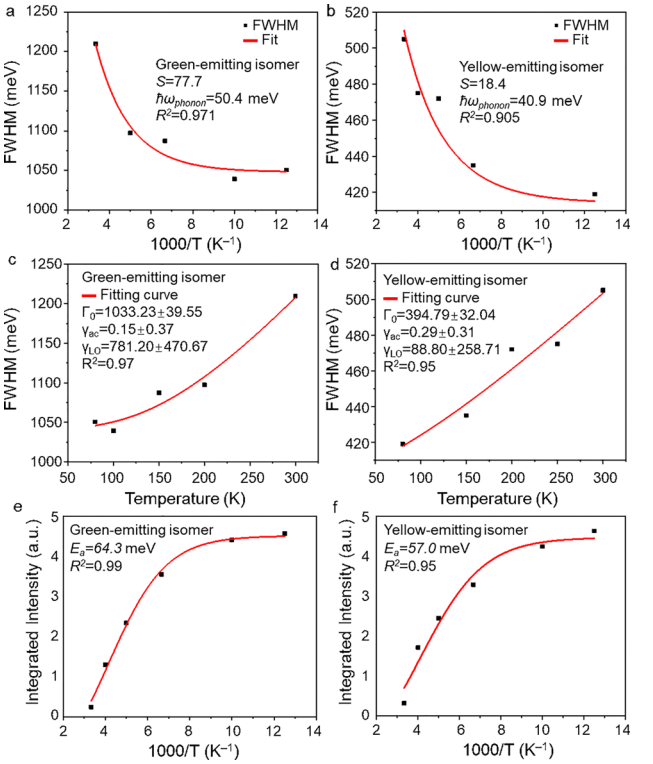

Fig. 4 Huang–Rhys factor estimation. (a) and (b) Plots of PL spectral widths (FWHM) of (a) green- and (b) yellow-emitting isomers *vs.* temperature, showing the Huang–Rhys factors (S). Electron–phonon estimation of (c) green- and (d) yellow-emitting isomers by fitting the FWHM of the PL profiles at different temperatures. Calculated activation energies (E_{a}) of the (e) green- and (f) yellow-emitting isomers.

Fig. 4e and f illustrates the Arrhenius plot of the inverse relationship between the integrated PL intensity and T (80–300 K), allowing for the estimation of the exciton binding energy using the equation $I(T) = \dfrac{I_0}{1 + A\exp\left(-\dfrac{E_{\mathrm{a}}}{k_{\mathrm{B}}T}\right)}$,[54] where I_0 is the PL intensity at 300 K, $I(T)$ is the PL intensity at temperature T, A is the Arrhenius constant, and E_{a} is the activation energy, which can be considered as the exciton binding energy (E_{b}). We estimated the E_{b} values for the green- and yellow-emitting isomers to be 64.3 meV and 57.0 meV, respectively, both of which are greater than the thermal energy at room temperature (26 meV).[55] Therefore, these findings provide strong evidence that the PL of the $(C_{10}H_{22}N_2)_4In_4Br_{20}$ isomeric crystals originates from exciton recombination rather than free carriers.

To clarify the intrinsic green and yellow emissions as well as the cracking- and photoinduced changes in the PL properties of the green-emitting isomer, we classify the emitting states into states governed by highly polar lattice phonons and shallow STE states (yellow-emitting) dominated by surface phonons, which are common to metal halides.[31,37] Therefore, the green emission originates from the lattice phonon-exciton-coupled states. In contrast, the intrinsic yellow emission is assigned to the surface phonon-exciton-coupled STE states. From a surface area perspective, the surface phonon density in an intact

microcrystal should be lower than the lattice phonon density, leading to green emission. Nevertheless, the short PL lifetime and the low PLQY of the green-emitting isomer suggest that the nonradiative recombination rate (k_{nrG}) dominates the relaxation of the excited state. However, when a crystal was cracked and photoactivated, the trapping rate (k_{t2}, Fig. 3d) and the detrapping rate (k_{dt}) result in a redshifted PL spectrum, a higher PL intensity, and a longer PL lifetime than the parent crystal.

Conclusions

This work demonstrates isomeric organic–inorganic indium bromide 0D single crystals $(C_{10}H_{22}N_2)_4In_4Br_{20}$, exhibiting fast green and delayed yellow emissions. The intrinsic differences in the PL colour, spectra, and lifetimes of these crystals are attributed to their lattice structures comprising ten identical $InBr_6$ octahedra in both lattices, four face-shared $InBr_4$ tetrahedra in the green-emitting isomer, and two unshared $InBr_4$ tetrahedra in the yellow-emitting isomer. Despite the distinct colours originating from crystal isomerism, relaxation from the green-to-yellow-emitting states, which provides delayed fluorescence, originates from strong exciton–phonon coupling, as derived from the activation energy and Huang–Rhys factor. These findings provided new insights into engineering isomeric 0D hybrid halide crystals with distinct PL colours, offering a foundation for developing next-generation optical devices.

Author contributions

H. Z. contributed to data curation, methodology and writing – original draft; H. Z., J. P., and V. B. contributed to the investigation and writing (reviewing and editing); H. Z., K. T., T. O., and J. P. contributed to formal analyses; H. Z., J. P. and V. B. contributed to conceptualization and validation. V. B. and J. P. contributed to funding acquisition and resources; and V. B. contributed to supervision.

Conflicts of interest

There are no conflicts to declare.

Data availability

All data supporting this work are present in the article and the Supplementary information (SI). Supplementary information: crystallographic parameters (Table S1), PXRD data and SCSRD structures (Fig. S1), SEM-EDX data (Fig. S2), DTA data (Fig. S3), absorption spectra and Tauc plots (Fig. S4), PLE spectra (Fig. S5), excitation power-dependent PL intensity and CIE data (Fig. S6), temperature-dependent PL spectra (Fig. S7), DFT data (Fig. S8), low-temperature PL spectra under 375 nm excitation and room temperature PL spectra under 365 nm excitation (Fig. S9), and PL decay parameters (Tables S2 and S3). See DOI: https://doi.org/10.1039/d5mh02322j.

CCDC 2514477 and 2514478 contain the supplementary crystallographic data for this paper.[56a,b]

Additional data related to this work may be obtained from the corresponding authors upon request.

Acknowledgements

This work was supported by the JSPS KAKENHI under grant number 23H01781 (V. B.). H. Z. acknowledges a Hokkaido University ExEx Doctoral Fellowship.

Notes and references

1 C. K. Moller, *Nature*, 1958, **182**, 1436.
2 M. V. Kovalenko, L. Protesescu and M. I. Bodnarchuk, *Science*, 2017, **358**, 745–750.
3 Q. A. Akkerman, G. Rainò, M. V. Kovalenko and L. Manna, *Nat. Mater.*, 2018, **17**, 394–405.
4 A. A. Kumar and N. Lee, *Mater. Horiz.*, 2025, **12**, 7749–7778.
5 Y. Asensio, L. Olano-Vegas, S. Mattioni, M. Gobbi, F. Casanova, L. E. Hueso and B. Martín-García, *Mater. Horiz.*, 2025, **12**, 2414–2435.
6 A. Kojima, K. Teshima, Y. Shirai and T. Miyasaka, *J. Am. Chem. Soc.*, 2009, **131**, 6050–6051.
7 A. K. Jena, A. Kulkarni and T. Miyasaka, *Chem. Rev.*, 2019, **119**, 3036–3103.
8 T. Leijtens, K. A. Bush, R. Prasanna and M. D. McGehee, *Nat. Energy*, 2018, **3**, 828–838.
9 M. Que, Y. Xu, Q. Wu, J. Chen, L. Gao and S. Liu, *Mater. Horiz.*, 2025, **12**, 2467–2502.
10 G. C. Xing, N. Mathews, S. S. Lim, N. Yantara, X. F. Liu, D. Sabba, M. Grätzel, S. Mhaisalkar and T. C. Sum, *Nat. Mater.*, 2014, **13**, 476–480.
11 H. M. Zhu, Y. P. Fu, F. Meng, X. X. Wu, Z. Z. Gong, Q. Ding, M. V. Gustafsson, M. T. Trinh, S. Jin and X. Y. Zhu, *Nat. Mater.*, 2015, **14**, 636–U115.
12 J. Moon, Y. Mehta, K. Gundogdu, F. So and Q. Gu, *Adv. Mater.*, 2024, **36**, 2211284.
13 Z. K. Tan, R. S. Moghaddam, M. L. Lai, P. Docampo, R. Higler, F. Deschler, M. Price, A. Sadhanala, L. M. Pazos, D. Credgington, F. Hanusch, T. Bein, H. J. Snaith and R. H. Friend, *Nat. Nanotechnol.*, 2014, **9**, 687–692.
14 J. Z. Ye, M. M. Byranvand, C. O. Martnez, R. L. Z. Hoye, M. Saliba and L. Polavarapu, *Angew. Chem., Int. Ed.*, 2021, **60**, 21636–21660.
15 H. Wang and D. H. Kim, *Chem. Soc. Rev.*, 2017, **46**, 5204–5236.
16 Y. Mo, X. Huang, Q. Hu, C. Hu, P. K. Chu and J. Li, *Mater. Horiz.*, 2025, **12**, 7221–7243.
17 T. B. Shonde, H. Liu, O. J. Olasupo, A. Bouchard, S. Bouchard, A. Franklin, X. Lin, L. M. Stand and B. Ma, *Mater. Horiz.*, 2024, **11**, 3076–3081.
18 W. Y. Gao, R. Huang, H. Dong, W. Y. Li, Z. B. Wu, Y. H. Chen and C. X. Ran, *Chem. Soc. Rev.*, 2025, **54**, 1384–1428.
19 X. Han, P. Cheng, R. Shi, Y. Zheng, S. Qi, J. Xu and X.-H. Bu, *Mater. Horiz.*, 2023, **10**, 1005–1011.

20 F. Hao, C. C. Stoumpos, P. J. Guo, N. J. Zhou, T. J. Marks, R. P. H. Chang and M. G. Kanatzidis, *J. Am. Chem. Soc.*, 2015, **137**, 11445–11452.
21 O. Xu, H. Peng, Q. Wei, L. Kong, X. Wang, H. Zhang, J. Zhao and B. Zou, *Mater. Horiz.*, 2025, **12**, 1596–1608.
22 S. Yu, H. Peng, Q. Wei, T. Li, W. Huang, X. He, Z. Du, J. Zhao and B. Zou, *Mater. Horiz.*, 2024, **11**, 2230–2241.
23 S. Attique, N. Ali, S. Ali, R. Khatoon, N. Li, A. Khesro, S. Rauf, S. K. Yang and H. Z. Wu, *Adv. Sci.*, 2020, **7**, 1903143.
24 X. Li, G. D. Zhang, Y. Q. Hua, F. C. Cui, X. Sun, J. X. Liu, H. J. Liu, Y. X. Bi, Z. J. Yue, Z. J. Zhai, H. B. Xia and X. T. Tao, *Angew. Chem., Int. Ed.*, 2023, **62**, 2315817.
25 Y. Liu, Y. P. Gong, S. N. Geng, M. L. Feng, D. Manidaki, Z. Y. Deng, C. C. Stoumpos, P. Canepa, Z. W. Xiao, W. X. Zhang and L. L. Mao, *Angew. Chem., Int. Ed.*, 2022, **61**, e202208875.
26 X. Q. Li, Z. S. Yue, F. Zhang, Q. X. Wang, Q. Y. Wei, Z. H. Sun, J. H. Luo and X. T. Liu, *Adv. Funct. Mater.*, 2024, **34**, 2311944.
27 T. Takenaka, K. Ishihara, M. Roppongi, Y. Miao, Y. Mizukami, T. Makita, J. Tsurumi, S. Watanabe, J. Takeya, M. Yamashita, K. Torizuka, Y. Uwatoko, T. Sasaki, X. Huang, W. Xu, D. Zhu, N. Su, J. G. Cheng, T. Shibauchi and K. Hashimoto, *Sci. Adv.*, 2021, **7**, eabf3996.
28 X. Y. Liu, F. Yuan, C. R. Zhu, J. R. Li, X. Q. Lv, G. C. Xing, Q. Wei, G. Wang, J. F. Dai, H. Dong, J. Xu, B. Jiao and Z. X. Wu, *Nano Energy*, 2022, **91**, 106664.
29 Y. Y. Ma, H. Q. Fu, X. L. Liu, Y. M. Sun, Q. Q. Zhong, W. J. Xu, X. W. Lei, G. D. Liu and C. Y. Yue, *Inorg. Chem.*, 2022, **61**, 8977–8981.
30 F. Zhang, D. W. Yang, Z. F. Shi, C. C. Qin, M. H. Cui, Z. Z. Ma, L. T. Wang, M. Wang, X. Z. Ji, X. Chen, D. Wu, X. J. Li, L. J. Zhang and C. X. Shan, *Nano Today*, 2021, **38**, 101153.
31 L. Zhou, J. F. Liao, Z. G. Huang, J. H. Wei, X. D. Wang, W. G. Li, H. Y. Chen, D. B. Kuang and C. Y. Su, *Angew. Chem., Int. Ed.*, 2019, **58**, 5277–5281.
32 D.-Y. Li, Y.-B. Shang, Q. Liu, H.-W. Zhang, X.-Y. Zhang, C.-Y. Yue and X.-W. Lei, *Mater. Horiz.*, 2023, **10**, 5004–5015.
33 Z. Tang, X. Meng, H. Y. Zhao, S. J. Ji, Q. J. Wang, T. X. Bai, R. L. Zhang, J. K. Jiang, C. Katan, J. Even and F. Liu, *Adv. Opt. Mater.*, 2024, **12**, 2301282.
34 F. Locardi, M. Cirignano, D. Baranov, Z. Y. Dang, M. Prato, F. Drago, M. Ferretti, V. Pinchetti, M. Fanciulli, S. Brovelli, L. De Trizio and L. Manna, *J. Am. Chem. Soc.*, 2018, **140**, 12989–12995.
35 Y. X. Zhao and K. Zhu, *Chem. Soc. Rev.*, 2016, **45**, 655–689.
36 J. J. Luo, X. M. Wang, S. R. Li, J. Liu, Y. M. Guo, G. D. Niu, L. Yao, Y. H. Fu, L. Gao, Q. S. Dong, C. Y. Zhao, M. Y. Leng, F. S. Ma, W. X. Liang, L. D. Wang, S. Y. Jin, J. B. Han, L. J. Zhang, J. Etheridge, J. B. Wang, Y. F. Yan, E. H. Sargent and J. Tang, *Nature*, 2018, **563**, 541.
37 Y. Yao, Y. Q. Peng, Z. H. Deng, W. Shen, M. Li, L. Zhou and R. X. He, *Inorg. Chem.*, 2024, **63**, 20878–20887.
38 J. H. Wei, J. F. Liao, L. Zhou, J. B. Luo, X. D. Wang and D. B. Kuang, *Sci. Adv.*, 2021, **7**, eabg3989.
39 P. Han, X. Mao, S. Yang, F. Zhang, B. Yang, D. Wei, W. Deng and K. Han, *Angew. Chem., Int. Ed.*, 2019, **58**, 17231–17235.
40 A. Mondal, M. Ubaid, S. Gupta, K. Pal and S. Bhattacharyya, *Angew. Chem., Int. Ed.*, 2025, **64**, 2412779.
41 N. Sun, J. W. Lin, S. H. He, J. D. Cao, Z. N. Guo, J. Zhao, Q. L. Liu and W. X. Yuan, *Inorg. Chem.*, 2023, **62**, 3018–3025.
42 H. Fattal, T. D. Creason, C. J. Delzer, A. Yangui, J. P. Hayward, B. J. Ross, M. H. Du, D. T. Glatzhofer and B. Saparov, *Inorg. Chem.*, 2021, **60**, 1046–1055.
43 L. Zhou, J. F. Liao, Z. G. Huang, J. H. Wei, X. D. Wang, H. Y. Chen and D. B. Kuang, *Angew. Chem., Int. Ed.*, 2019, **58**, 15435–15440.
44 S. L. Kang, Q. Q. He, Y. Q. Shen, W. H. Ning and Y. Fang, *Inorg. Chem.*, 2025, **64**, 4035–4042.
45 D. Y. Li, H. Y. Kang, Y. H. Liu, J. Zhang, C. Y. Yue, D. P. Yan and X. W. Lei, *Chem. Sci.*, 2024, **15**, 953–963.
46 A. S. Kshirsagar, Y. Singh, U. M. Kuruppu, B. Donnadieu, N. Rai and M. K. Gangishetty, *Chem. Mater.*, 2022, **34**, 10928–10939.
47 X. L. Song, S. H. Wang, Y. Yang, Y. L. Zhou, X. Huang, B. Tang and H. M. Liu, *Chem. Mater.*, 2024, **36**, 7744–7753.
48 L. P. Du, Q. W. Zhou, Q. Q. He, Y. Liu, Y. Q. Shen, H. J. Lv, L. L. Sheng, T. Cheng, H. Yang, L. Wan, Y. Fang and W. H. Ning, *Adv. Funct. Mater.*, 2024, **34**, 2315676.
49 Y. L. Liu, Y. Wei, Z. S. Luo, B. Xu, M. Y. He, P. B. Hong, C. Li and Z. W. Quan, *Chem. Sci.*, 2024, **15**, 15480–15488.
50 K. Zhang, Y. Shen, L. X. Cao, Z. H. Su, X. M. Hu, S. C. Feng, B. F. Wang, F. M. Xie, H. Z. Li, X. Y. Gao, Y. Q. Li and J. X. Tang, *Nat. Commun.*, 2024, **15**, 10621.
51 L. Zhou, J. F. Liao and D. B. Kuang, *Adv. Opt. Mater.*, 2021, **9**, 2100544.
52 Y. Liu, F. Di Stasio, C. H. Bi, J. B. Zhang, Z. G. Xia, Z. F. Shi and L. Manna, *Adv. Mater.*, 2024, **36**, 2312482.
53 C. Du, Z. Q. Huang, J. Zhou, J. Y. Su, P. Yu, Z. Q. Zheng, J. H. Yan, J. D. Yao, Y. C. Chen and X. M. Duan, *Adv. Mater.*, 2025, **37**, 2410417.
54 F. Zhang, Z. H. Zhao, B. K. Chen, H. Zheng, L. L. Huang, Y. Liu, Y. T. Wang and A. L. Rogach, *Adv. Opt. Mater.*, 2020, **8**, 1901723.
55 J. Zhang, Y. Yang, H. Deng, U. Farooq, X. Yang, J. Khan, J. Tang and H. Song, *ACS Nano*, 2017, **11**, 9294–9302.
56 (*a*) CCDC 2514477: Experimental Crystal Structure Determination, 2026, DOI: 10.5517/ccdc.csd.cc2qdj5v; (*b*) CCDC 2514478: Experimental Crystal Structure Determination, 2026, DOI: 10.5517/ccdc.csd.cc2qdj6w.

